3-7-2018

Comparison of Plume Dynamics for Laser Ablated Metals: Al and Ti

William A. Bauer
Air Force Institute of Technology

Glen P. Perram
Air Force Institute of Technology

Timothy Haugan
Air Force Research Laboratory

Recommended Citation

Bauer, W., Perram, G. P., & Haugan, T. (2018). Comparison of plume dynamics for laser ablated metals: Al and Ti. Journal of Applied Physics, 123(9), 095304. https://doi.org/10.1063/1.5011028

Journal of Applied Physics

RESEARCH ARTICLE | MARCH 06 2018

Comparison of plume dynamics for laser ablated metals: Al and Ti

William Bauer; Glen P. Perram; Timothy Haugan

Journal of Applied Physics 123, 095304 (2018)
https://doi.org/10.1063/1.5011028

Comparison of plume dynamics for laser ablated metals: Al and Ti

William Bauer,[1] Glen P. Perram,[1,a)] and Timothy Haugan[2]
[1]*Department of Engineering Physics, Air Force Institute of Technology, Wright Patterson AFB, Ohio 45433, USA*
[2]*Aerospace Systems Directorate, Air Force Research Laboratory, Wright-Patterson AFB, Ohio 45433, USA*

(Received 29 October 2017; accepted 13 January 2018; published online 6 March 2018)

Emissive plumes from pulsed laser ablation of bulk Ti and Al from KrF laser irradiation at laser fluence up to 3.5 J/cm^2 and argon background pressures of 0–1 Torr have been observed using gated intensified charged-coupled device imagery. Mass loss for Ti increases from 0.1 to 0.8 μg/pulse as pulse energy increase from 174 to 282 mJ/pulse (35–170 photons/atom) and decreases by ~30% as pressure increases from vacuum to 1 Torr. Early plume energies are described by the free expansion velocities of 1.57 ± 0.02 and of 1.81 ± 0.07 cm/μs for Ti and Al, respectively, and up to 90% of the incoming laser energy can be attributed to the Al shock front in the mid-field. The ablation thresholds of 90 ± 27 mJ (1.12 ± 0.34 J/cm^2) for Ti and 126 ± 13 mJ (1.58 ± 0.16 J/cm^2) for Al also represent 30%–70% of the incident laser energy. The decrease in mass loss at higher pressures is attributed to plasma shielding of the target surface. https://doi.org/10.1063/1.5011028

I. INTRODUCTION

The laser ablation and emissions plume creation process is complex, encompassing melting and vaporization of the target surface, generation of a plasma from the established vapor plume, laser absorption of the incoming laser radiation by the plume, and expansion of the plume away from the target surface.[1,2] These laser-induced plasmas are highly ionized,[3] expand into the background gas with shock speeds of >1 cm/μs,[4,5] and exhibit hydrodynamic phenomena such as plume splitting and Rayleigh–Taylor instabilities.[6–11]

Knowledge of the plume dynamics is essential for the pulsed laser deposition (PLD) of thin films where a substrate is typically placed 1–20 cm from the target in a background pressure of 0.1–1.0 Torr.[2] Pulsed laser deposition of titanium is increasingly utilized to create nitonol coatings for orthopedic implants,[8] nitrogen-doped titanium oxide for photocatalysts,[9] and TiN layers for diffusion barriers in microelectronics and tribological coatings for high speed tools.[10] The production of molecular constituents and nanoparticles[6,7,11–13] usually requires slowing the plume by incorporating rare gas, nitrogen, or oxygen background gases, with plume stopping distances located near the substrate. Laser-induced breakdown spectroscopy (LIBS) produces similar plumes, but propagate shorter distances and evolve more rapidly due to the higher atmospheric pressure conditions.[14] In the present study, we compare the plume dynamics for pulsed laser ablation of two common aerospace metals, Al and Ti.[15,16] Laser cutting, welding, and additive manufacturing using Al or Ti depend on the understanding of the laser material interaction, typically at lower irradiance.[16] The response of these metals to high-power laser radiation is also important for the effectiveness of emerging laser weapon systems.[15]

Experimental characterization of laser ablated plumes and corresponding shockwaves have been conducted using shadowgraphy,[17,18] optical emission spectroscopy,[19–21] charge collection devices,[4,22–24] and laser-induced fluorescence.[5,25] These techniques offer insights into the plume expansion process and its constituents but provide limited information regarding the structure of the emissive plume. Fast visible emissions imaging through the use of intensified charged-coupled device (ICCD) arrays has been extensively utilized to image laser ablation plumes.[2,26–29] ICCD imaging offers the advantage of being able to record the structure of the emissive plumes in a 2D image with ~1 ns temporal resolution and ~100 μm spatial resolution. The pulsed ablation of aluminum has been studied in some detail, including Nd:YAG sources at 1.06 μm,[18,27,29,30] sources with greater than 1 ns duration at shorter wavelengths,[13,31–34] and short pulse (fs) sources.[35] Background gases of air, rare gases, and nitrogen at pressures up to atmosphere have been examined, with plume stopping distance reported for low pressure nitrogen backgrounds,[29] and expansion dynamics characterized at atmospheric pressures.[18,27,36] The scaling of Al plume dynamics and mass loss for UV laser sources is largely unstudied. Pulse laser ablation of titanium has received considerably less attention, with the studies limited to short pulse effects in vacuum,[10] deposition of nitonol films in vacuum,[8] and LIBS at 532 nm.[37] In the present study, we seek to compare the plume dynamics for Al and Ti targets irradiated at 248 nm to examine the influence of atomic momentum on plume thickness and plume slowing and resolve plume structure for low argon background pressures. In addition, we compare the dependence of mass removal on laser fluence and background pressure with the plume energy driving shock formation. This systematic study of ablated mass and plume dynamics will be used to better understand the implications of background pressure scaling relationships. By defining the background pressure conditions for well-formed plume fronts, future studies of evolving velocity distributions, shock front instabilities, and translational-to-electronic excitation rates is enabled.

II. EXPERIMENTAL DETAILS

A schematic of the experimental apparatus is presented in Fig. 1; further details of the experiment have been

a)Author to whom correspondence should be addressed: glen.perram@afit.edu

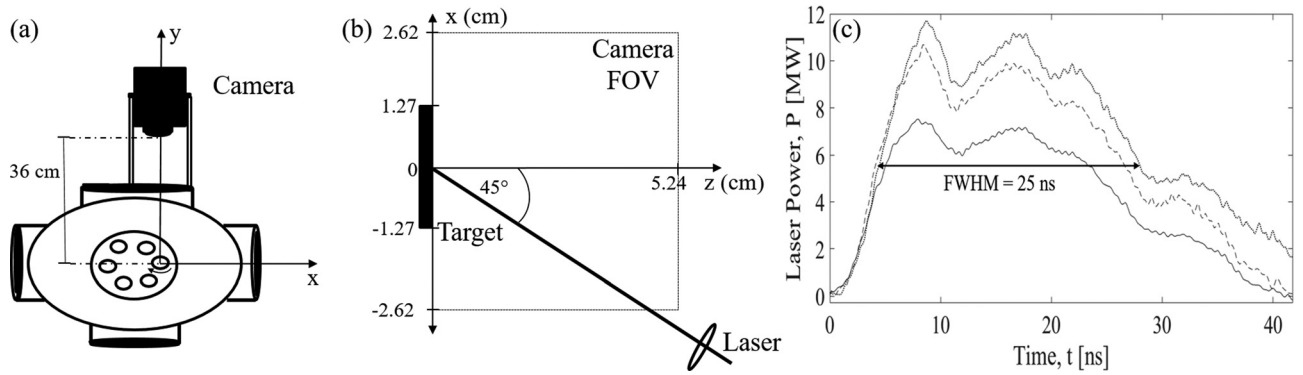

FIG. 1. Experiment apparatus in (a) x–y plane (b) and x–z plane (dimensions specific to 50 mm lens imaging system) and (c) laser pulse shape for (.) 282 mJ/pulse, (– –) 240 mJ/pulse, and (–) 174 mJ/pulse.

reported previously.[38] Briefly, a Lambda Physik LPX 305 KrF laser at $\lambda = 248$ nm delivered up to 282 mJ/pulse on the target in an 8×1 mm rectangular spot with a repetition rate of 1 Hz. The plume propagates normal to the target in the z-direction, and the gated camera observes the plume from above, integrating along the y-direction. The pulse exhibits a FWHM of 25 ns and a rise time of 5 ns, yielding an intensity of 141 MW/cm^2. The damaged area as observed by optical microscopy is similar to the laser footprint, as shown in Fig. 2. The laser beam is focused onto the target inside the 10″ vacuum chamber through a 300 mm focal length plano-convex fused silica 2″ lens at an angle of incidence of ∼45° to the target normal. The chamber was evacuated to a base pressure of 10^{-6} Torr with a turbomolecular pump before being backfilled with the desired pressure of 99.999% Ar (50, 250, 500, and 1000 mTorr). Pressures were monitored by a capacitance manometer with a 1–1000 mTorr range (±0.5% of reading) and an ionization gauge for near vacuum conditions.

The targets were Kurt Lesker of 1″ diameter by 0.25″ thick sputtering targets typically of either 99.99% Al or 99.7% Ti. Targets were mounted onto a carousel, allowing up to six targets into the chamber at one time. Each of the targets is rotated at 10 rpm about the z-axis during laser irradiation to reduce surface cratering. Laser energy delivered to the target was measured by utilizing a Coherent LMP10I detector calibrated to a wavelength of 248 nm positioned inside the target chamber. Images suffer from <5% pulse-to-pulse laser flicker and ≤10 ns pulse-to-pulse laser timing jitter. Typical thermal and optical properties of Al and Ti are provided in Table I.

Fast visible emission images were captured utilizing a Princeton Instruments PIMAX I intensified charged-coupled device (ICCD). The 512×512 array PIMAX I was equipped to image early delays and short plume distance emissions with a Nikon AF Nikkor 60 mm micro f/2.8 lens that provided a field of view (FOV) of 5.24×5.24 cm (0.102 mm per pixel) or to image longer time/farther spatial distance plume details when equipped with a Nikon AF Nikkor 50 mm f/1.4 lens that provided a FOV of 8.28×8.28 cm (0.162 mm per pixel). The point spread function has been characterized and is somewhat larger, 0.5 mm for the 60 mm imaging system and 1.1 mm for the 50 mm imaging system.[38] The camera was gated with integration times ranging from 2 to 150 ns and delays of up to ∼12 μs after the onset of irradiation. Both the widths and delays were varied nonlinearly over 100 shots, and the laser electronics were utilized to trigger the camera. For the initial plume speeds of ∼2 cm/μs presented below, the 2 ns integration time implies a 40 μm or 0.39 pixel motion during image capture. The plume slows and decreases in intensity at later times, allowing for the longer integration times to improve the signal to noise ratio, with <4 pixel motion during the image capture. The 16 bit camera saturates at 65 536 counts with a dark signal of 68 counts. The PIMAX camera quantum efficiency is above 20% from 410 to 890 nm, with a maximum quantum efficiency of ∼40% at approximately 700 nm. Band pass filters were employed to isolate the emission from

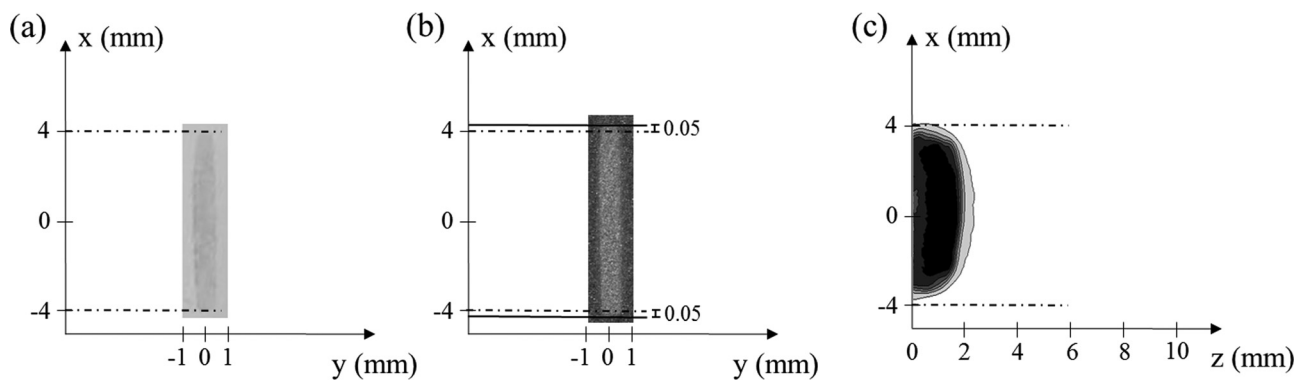

FIG. 2. (a) Laser spot at target from thermal paper burn pattern, (b) optical microscope image of Ti damage, and (c) Ti 224 mJ/pulse ablation plume in 500 mTorr Ar at 141 ns delay.

TABLE I. Ti and Al material properties.[1,39] φ_i is the angle of incidence.

	Al	Ti
Molar mass, M (g/mol)	26.98	47.87
Density, ρ (g/cm^3)	2.7	4.506
Melting temperature, T_m (K)	933	1943
Vaporization temperature, T_v (K)	2792	3560
Enthalpy of melting, ΔH_m (J/g)	397	295.6
Enthalpy of vaporization, ΔH_v (J/g)	10 896	8800
Spectral reflectance, R ($\lambda = 248$ nm, $\varphi_i = 0°$)	0.9244	0.236
Heat capacity, Cp (J/g K) (T = 300 K)	0.9	0.52
Thermal diffusivity, D (cm^2/s) (T = 300 K)	0.98	0.093
Absorption coefficient, α (cm^{-1}) ($\lambda = 248$ nm)	1.49×10^6	6.13×10^5
Ionization potential, I (eV)	5.99	6.83

neutral and ion atomic species.[38] The broadband emissions include $\leq$10 lines for Ti and four lines for Al, with the dominant lines exhibiting radiative rates of $\geq 6 \times 10^7$ s^{-1}.[40] Plume motion during a radiative lifetime for the faster emitters is 0.4 mm, resulting in the conclusion that emission is produced locally (within 4 pixels).

An example of the plume image shortly after the laser pulse is shown in Fig. 2(c). The plume lateral extent at the target matches the laser footprint. The plume has expanded to $z = 2.4$ mm in 141 ns, yielding an initial velocity of $\sim$1.7 cm/μs. At the end of the laser pulse, $t = 25$ ns, the plume volume is $\sim$3.4 mm^3.

Mass loss experiments were performed with a Mettler Toledo XP26 microbalance (minimum resolution of 0.001 mg) as functions of pressure and laser energy. The $\sim$14.5 g Ti and $\sim$8.8 g Al samples were received from the vendor sealed in Ar. They were opened under atmospheric conditions and allowed to oxidize and hydrolyze until stable ($\sim$30 min) with mass increases of 44 μg and 56 μg for Ti and Al, respectively. Samples were weighed on the XP26 before being placed into the chamber for irradiation. The chamber was evacuated to base pressure for at least 12 h before being backfilled with the desired amount of Ar. Samples were irradiated for 600 shots at 1 Hz with the sample rotating about the z-axis before being removed and then re-weighed on the XP-26. Samples were measured a minimum of 5 times on the XP-26 before and after irradiation with a variance of $<$1%. All results were averaged equally over the 600 shots to determine the amount of mass loss per pulse.

TABLE II. Mass removal parameters.

Metal	Ar pressure (Torr)	Δm/ΔE (μg/J)	E_{th} (mJ)	Φ_{th} (J/cm^2)
Ti	0	3.85 ± 0.71	90 ± 27	1.12 ± 0.34
Ti	0.5	4.92 ± 0.83	138 ± 17	1.73 ± 0.21
Ti	1.0	6.34 ± 0.12	156 ± 1.6	1.95 ± 0.20
Al	0	4.72 ± 0.58	126 ± 13	1.58 ± 0.16
Al	1.0	3.02 ± 0.70	144 ± 21	1.80 ± 0.26

III. RESULTS AND DISCUSSION

A. Mass loss

The amount of material ablated per pulse as a function of laser energy and background pressure for both Al and Ti targets is summarized in Fig. 3 and Table II. Generally, more material was ablated from both targets with increasing laser energy. The maximum Ti mass removed of 0.80 μg/pulse ($\sim$482 μg in 600 pulses) occurs at the greatest delivered energy of 282 mJ, corresponding to 35 laser photons (175 eV) per ablated atom. The amount of mass ablated from a typical Ti target was on average 49% higher than the amount ablated for Al. However, due to its higher molar mass, 26% fewer Ti atoms are produced than Al, consistent with the lower melting and vaporization temperatures of Al.

The mass removal reported in Fig. 3 is similar to the previous results, although the exact conditions of the experiments in this study are not replicated elsewhere. Sdorra *et al.* reported Al mass loss of 0.5 μg per pulse from the 4th harmonic of an Nd:YAG laser ($\lambda = 266$ nm) at 3.2 GW/cm^2 for an Al target in 100 Torr of Ar using optical microscopy.[41] Iida reported Al mass loss of 0.33 μg per pulse from the 1st harmonic of an Nd:YAG laser ($\lambda = 1064$ nm) at 9.5 GW/cm^2 in 0.1 Torr Ar using a microbalance.[42] Torrisi *et al.* ablated Al with the second harmonic of an Nd:YAG laser ($\lambda = 532$ nm) in vacuum and recorded results of 0.28 μg at 170 mJ/pulse laser energy.[43] Timm *et al.* reported a mass loss for the closest conditions to those of this work. KrF ablation of Al and Ti at 0.12–1.6 GW/cm^2 at vacuum pressure was performed and mass losses of $\sim$0.02 μg of Al and $\sim$0.1 μg of Ti at 0.19 GW/cm^2 were recorded using a gravimetric balance and averaging over multiple shots.[44] Their results appear to be lower than those recorded in this study and the results of the other two studies.

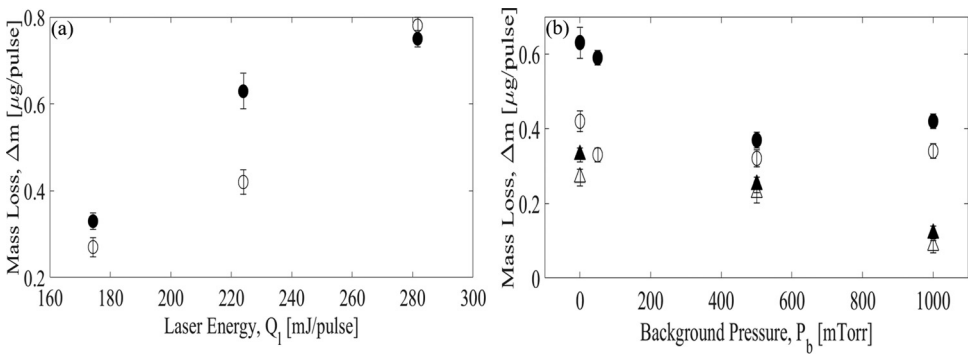

FIG. 3. (a) Dependence of mass loss on laser energy (●) Ti and (○) Al at vacuum, and (b) dependence of mass loss on background pressure (▲) Ti 174 mJ/pulse, (●) Ti 224 mJ/pulse, (△) Al 174 mJ/pulse, and (○) Al 224 mJ/pulse.

Figure 3(b) illustrates less mass ablated at higher background pressure. This observation is further supported through a determination of Ti mass removal rates using linear fits of mass removed as a function of laser energy for varying background pressures (Table II). The average increase in Ti mass removal with laser fluence is $5.03 \pm 0.37\ \mu$g/J, with pressure-specific results provided. While linear fits are not fully justified due to the plume shielding and other laser target interactions, the limited sampling and modest range in delivered fluence do not justify a more complex relationship. Error bounds in Table II and the remainder of this paper reflect the statistical 1σ error in the fit parameter. While the mass loss results in Fig. 3(b) generally decreased with increasing background pressure, one exception to this trend is the Ti ablation mass loss results at 282 mJ/pulse, which is not displayed. In this case, a mass loss of $0.78 \pm 0.03\ \mu$g is observed, independent of background pressure. While the statistical error bound is small, it is possible that an unknown systematic error might contribute to this anomalous result.

Extrapolations of the linear response of ablated mass with laser energy to zero mass reveal ablation thresholds of $\Phi_{th} = 1$–$2\ \mathrm{J/cm^2}$. Ablation thresholds are often calculated using the energy required to bring a volume of target material to a specified temperature[1,45,46]

$$E_{th} = \frac{A\rho(\Delta H)\left(\alpha^{-1} + \sqrt{D\tau_{laser}}\right)}{(1-R)}, \tag{1}$$

where the material properties are defined in Table I, and the enthalpy change may include heat capacity and latent heats for melting and vaporization. The details for the evolving reflectivity at elevated temperatures and the temporal evolution of the ablated mass are not addressed in Eq. (1), but the result is an adequate approximation that correlated the thresholds for many metals.[47] Using the heat of vaporization only and excluding reflection yields thresholds of 1.98 and $4.7\ \mathrm{J/cm^2}$ for Ti and Al, respectively. Observed thresholds for ns ablation sources at various wavelengths range from 2 to $2.4\ \mathrm{J/cm^2}$ for Ti[6,44] and 2.3 to $3.6\ \mathrm{J/cm^2}$ for Al.[34,44,47]

As the Ar pressure increases from vacuum to 1 Torr, the apparent Ti fluence threshold increases by 66 mJ. Prior studies attributed a significant decrease in mass loss at higher background pressure to plume confinement and increased laser shielding of the target.[42,48] Assuming negligible particle re-deposition (see discussion below), the 66 ± 27 mJ increase in the apparent fluence threshold represents a $28 \pm 11\%$ increase in shielding of the target surface.

It has been observed that particle re-deposition increases with increasing background pressure during UV metal laser ablation, offering a second explanation for the results of Fig. 3(b).[49] Visible inspection of post-irradiated samples show that samples irradiated in vacuum exhibit deeper looking ablated laser spots than do samples at higher pressure, indicating a higher rate of ablation at lower pressure. Optical microscopy of the post-irradiated samples does not exhibit obvious re-deposited material. Furthermore, the samples were swabbed to determine qualitatively if re-deposition was present. Very faint amounts of debris were observed on some Ti and Al sample swabs, with no apparent trend due to pressure or laser energy. Finally, the analysis of the plume dynamics from the imaging, discussed in Sec. III C, provides additional insights into this topic. It will be observed that the plume accelerates during the laser pulse, the initial plume kinetic energy declines at higher background pressures, and the shock front expansion does not properly scale with a constant plume mass. Eventually, it will be concluded that plume shielding rather is more significant than mass re-deposition.

B. Plume imagery

Gated imagery reveals key information regarding the shock development, plume kinetic energy, and evolution of velocity distributions. The qualitative features of the plume imagery are now examined. Typical fast visible imaging contour plots of KrF ablation of Ti at 1000 mTorr are presented in Fig. 4. The intensities in each frame are normalized to the maximum observed for that individual gate to highlight the relative features. The initial plume size matches the laser spot and damage area. The Ti emissions expand into

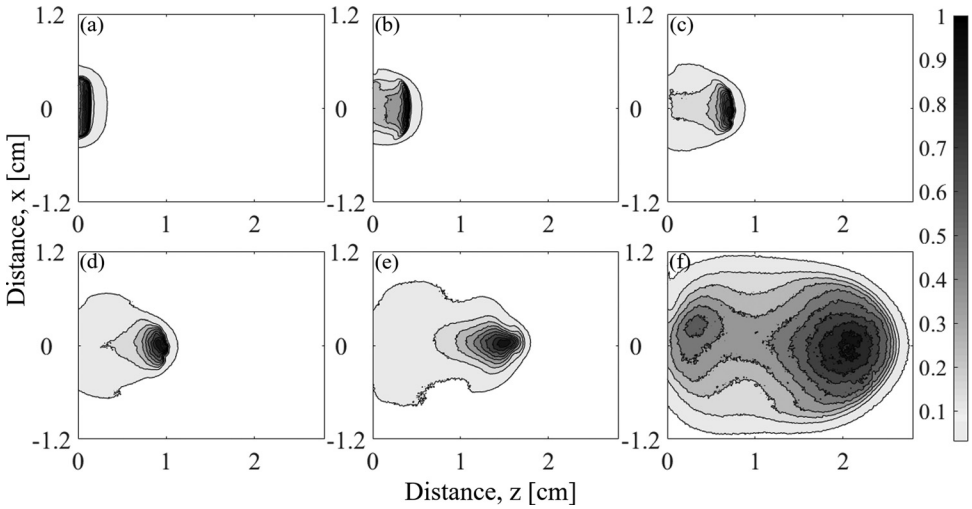

FIG. 4. Intensity contour images of Ti ablation at 224 mJ 1000 mTorr Ar at (a) 97 ns, (b) 295 ns, (c) 684 ns, (d) 1.13 μs, (e) 2.8 μs, and (f) 9.85 μs delay times.

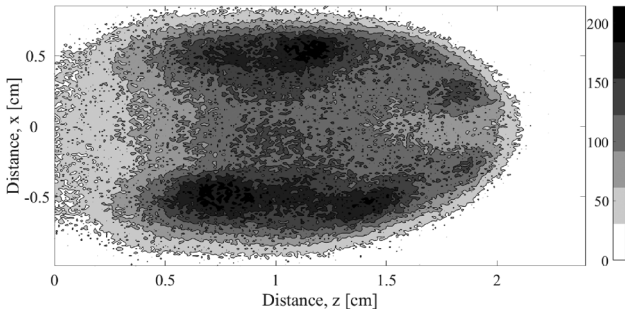

FIG. 5. Intensity contours of 224 mJ Al ablation in 500 mTorr Ar at 6.1 μs delay showing vortices as plume slows.

the Ar background at an initial velocity of $\sim$1.6 cm/μs. At $\sim$10 μs, the plume has reached its stopping distance of 2.8 cm.

The Al ablation plume follows the same general plume dynamics as Ti. However, Al slows more rapidly because it loses relatively more momentum per collision due to its lower molar mass (assuming both Al and Ti initially expand at comparable speeds). In Fig. 5, the plume comes to shorter stopping distance, 2.1 cm, at earlier time despite the lower pressure. Hydrodynamic vortices are readily observed as the plume slows due to collisions with the background gas and circles around the lower pressure edges of the plume. The rotational rate was estimated to be 8.3×10^5 rad/s at a radius of approximately 1.7 cm measured from the target surface.

Filtered ICCD images allow for capturing spectrally resolved images and monitoring the evolution of selected emitters.[7,50] Spectral data from 300 to 800 nm was previously recorded using the present apparatus, identifying neutral and singly ionized species.[38] Narrow band pass filters ($\leq$10 nm bandwidth) with center wavelengths of 500 nm, 375 nm, 394 nm, and 560 nm were utilized to isolate emission from neutral and singly ionized Ti and Al.[38] Figure 6 illustrates intensities along the centerline of the plume for both Ti and Al ablation detailing the location of the neutral and ionized species. Also shown are the unfiltered, broadband intensities, which decrease for longer delays. The filtered data intensity is lower than the broadband signal, reflecting the narrow spectral bandwidth and the low detector sensitivity at wavelengths below 400 nm. Data in each figure were scaled to the broadband signal with average scaling factors provided in each figure.

At early times, the ion and neutral distributions evolve quite differently. Most striking is the earliest time distributions for Ti in Fig. 6(a) where the broadband emission extends much farther from the target than both the neutral and ion images. Because the filters cover a small fraction of the emission particularly for the dense Ti visible spectrum, it is possible that this intensity is due to other excited electronic states.[38] No appreciable emissions from highly charged Ti ions or from the Ar background were detected in the current studies using a non-imaging grating spectrometer, consistent with other similar Ti ablation studies.[5,19,38] At larger fluences, highly charged metallic ions have been previously observed[20,51] and might contribute to the broadband imagery. A broad-spectrum continuum emission—Bremsstrahlung radiation—is produced via free-free transitions in the plasma and exists for the first 1–2 mm of expansion.[2,52,53] At 350 ns [Fig. 6(b)], the broadband and Ti I species share a common contact front, but the neutral emission is highest near the target. At times of $>$0.5 μs [Figs. 6(c) and 6(f)], the neutral, ion, and broadband profiles for both Ti and Al share a common spatial distribution. The Al

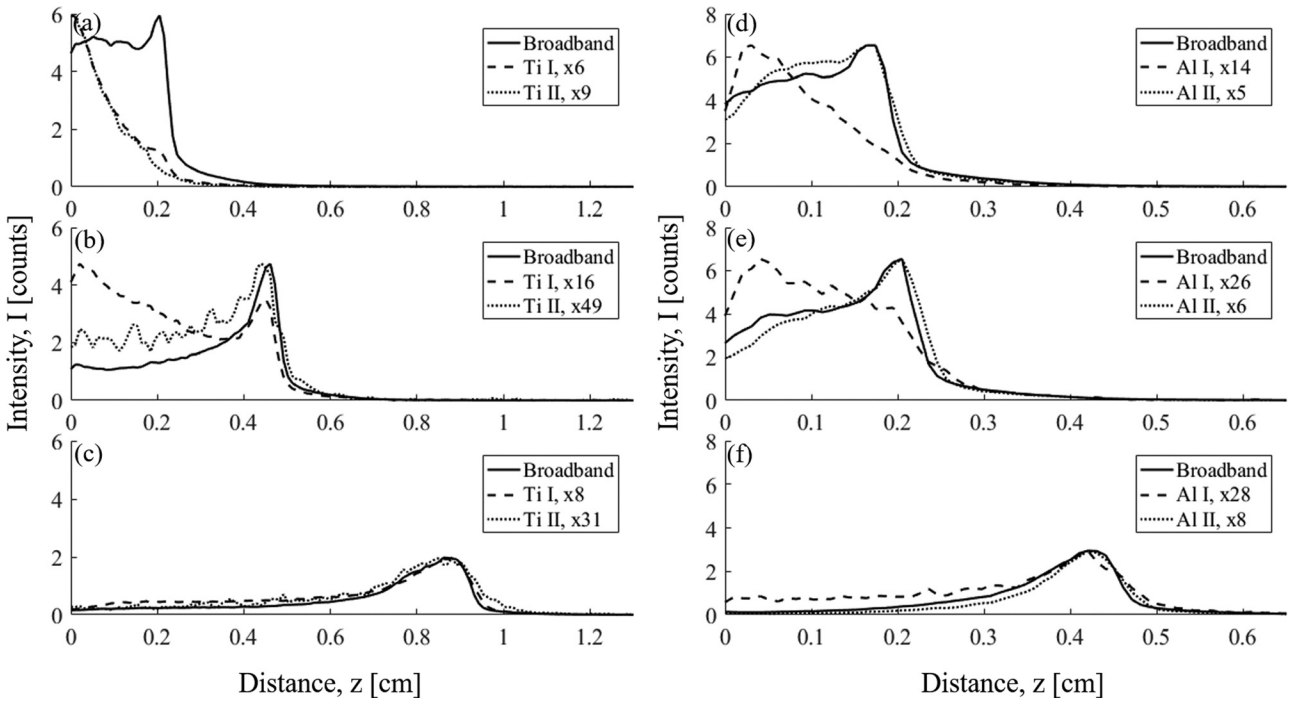

FIG. 6. Centerline intensity for 224 mJ 1000 mTorr Ti ablation at (a) 145 ns, (b) 350 ns, and (c) 940 ns and for 224 mJ 1000 mTorr Al ablation at delays of (d) 135 ns, (e) 160 ns, and (f) 390 ns. Solid lines represent broadband signals, dashed lines represent the excited neutral species (Ti I or Al I), and dotted lines represent the excited ionized species (Ti II or Al II).

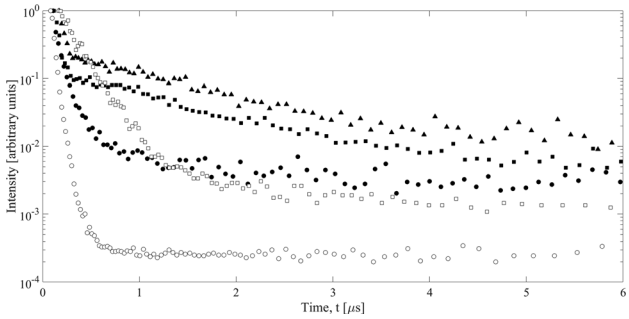

FIG. 7. Filtered imaging intensity dependence on time for Ti II in (●) vacuum, (▲) 500 mTorr, and (■) 1000 mTorr and for Al II in (○) vacuum and (□) 1000 mTorr.

intensity sequence [Figs. 6(d)–6(f)] also shows the neutral species (Al I) dwelling at the surface, while the ionized species (Al II) peaks at the broadband contact front at earlier delays. At times of >240 ns, the Al I species appears to have reached the contact front and joined the Al II signal.

Filtered imaging intensity data reveal that the ion signal persists longer in ambient pressure than in vacuum. Figure 7 shows that the Ti II signal lasted for ∼1 μs under expansion into vacuum where no shock front is established. Conversely, the Ti II signal lasted for >5 μs during expansion into 500 mTorr and 1000 mTorr of Ar. The Al II signal showed the same trend but at different delays. With a plume expansion of ∼1 cm/μs even at target distances of >1 cm, the kinetic energy is sufficient to produce ionization. The ionization potential for Ti is higher than for Al, possibly explaining the higher Al II signal far from the target at short delays.[39] Optical emission and ion probe studies have observed that ions generally precede the neutral species in the emissive plume.[51]

The ablated plume shapes are significantly affected by the background pressure. Figure 8 shows images of Ti ablation plumes under varying background pressures at 1.1 μs delay. The corresponding intensity profiles along the centerline of the plume in the *z*-direction are also provided. At vacuum background pressure, a well-established contact front is not observed for either Ti or Al ablation due to the lack of background gas atoms to excite and slow the leading edge of the plume. Strong shock fronts are clearly observed in the higher background pressure cases. Since the radiative rates are rapid, 10^7–$10^8\ s^{-1}$, the emission largely occurs in the same pixel that the excitation originated. That is, the excited states are not propagated in the *z*-direction, and the emission is produced locally. As pressure increases, more background gas is displaced, a stronger contact front develops, and the plume slows.

At 500 mTorr, the thickness of the contact front is $\delta = 0.4$ mm, nearly the same as the mean free path. The speed of sound in Ar, v_{Ar}, at 294 K is 319 m/s. The corresponding contact front location, $z = 1.3$ cm, for the 1.2 μs delay established a velocity of 1.08 cm/μs or a local Mach number of M = 34. Figures 8(g) and 8(h) reveal that the contact front in 1 Torr has slowed to 0.95 cm/μs, while the front thickness is approximately the same as 500 mTorr ($\delta = 0.5$ mm). At these higher-pressure conditions, the plume has suffered sufficient collisions to begin to dissipate the over-pressure and the plume is quickly slowing.

Figure 9 shows the Ti emissive plume dependence on laser energy. The leading edge distance traveled by the plume increases with increasing laser energy. The intensity of the plume increases by >400% when increasing laser energy by 108 mJ/pulse. The shape of the plume appears to be approximately equivalent.

C. Dependence of plume dynamics on pressure and laser energy

The kinetic energy of the expanding plume depends on the physical properties of the irradiated metal, laser energy, and background pressure, and can be characterized from the plume imagery. The trajectory of the shock front, *z(t)*, defined by the location of the emissive front at 10% of the maximum intensity, is illustrated during the time when the laser pulse is on in Fig. 10 and for a few cases after the laser pulse in Fig. 11.

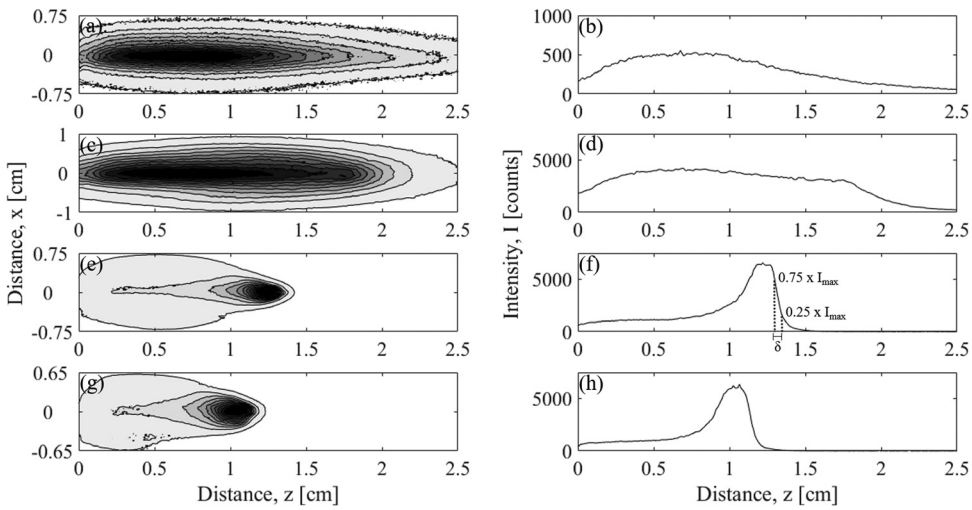

FIG. 8. Ti ablation intensity contour images and intensity along the centerline of the plume at 240 mJ/pulse laser energy and Ar pressures of (a) and (b) vacuum, (c) and (d) 50 mTorr, (e) and (f) 500 mTorr, and (g) and (h) 1 Torr at 1.2 μs delay. Contact front thickness (δ) is defined as the distance between the 25% and 75% of maximum intensity (I_{max}) at the plume leading edge.

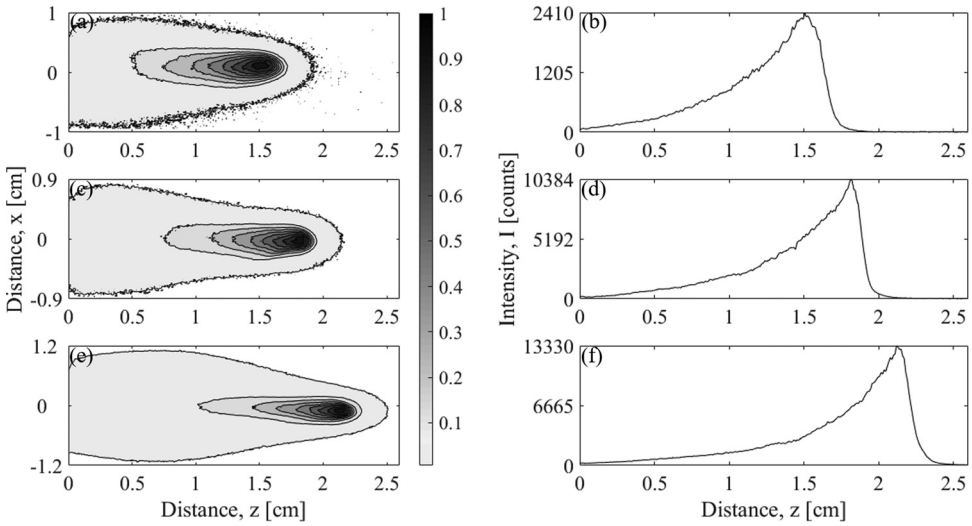

FIG. 9. Ti ablation intensity contour images and intensity along the centerline of the plume at 500 mTorr Ar at (a) and (b) 174 mJ/pulse, (c) and (d) 224 mJ/pulse, and (e) and (f) 282 mJ/pulse at 2.8 μs delay.

The plume expansion during the laser excitation shown in Fig. 10 clearly indicates interaction of the plume with the laser radiation. The plume initially expands in a manner consistent with the ~40 ns temporal energy distribution of the laser pulse. A fit of the linear portion of the trajectory from 10 ns to 30 ns results in a velocity of 5.8 cm/μs. When coupled with the mass loss results from Sec. III A, kinetic energies ranging from 0.6 to 1 J are calculated, three to four times the incoming laser energy. Because calculation of the kinetic energies using the *ex situ* mass loss data violate conservation of energy, clearly the mass involved in the earliest expansion of the plume during the laser pulse is significantly less than the total mass loss given in Fig. 3. That is, the mass ejection rate is highest late in the ablation process, and these atoms receive less kinetic energy. Indeed, the free expansion velocity for the full plume is much lower (~1.6 cm/μs), and when coupled with the total mass loss, data given in Fig. 3 result in kinetic energies that do not violate energy conservation, as discussed below. Laser-plume coupling mechanisms such as inverse-Bremsstrahlung and photoionization are well established in literature.[1,52] Furthermore, early plume expansion mechanisms have been postulated describing the rapid acceleration of ions due to a coulombic attractive force from electrons that have been accelerated away from the plume.[46,51,54] A thorough determination of a laser plume coupling mechanism responsible for the observed laser-plume expansion is beyond the scope of this paper, and the experimental findings are simply noted here.

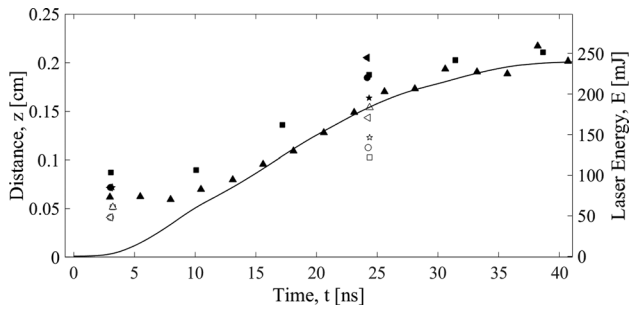

FIG. 10. Ti (filled markers) and Al (unfilled markers) plume trajectories reflecting the 240 mJ laser pulse temporal distribution (–) at (●) vacuum, (■) 50 mTorr, (★) 250 mTorr, (▲) 500 mTorr, and (◀) 1000 mTorr Ar.

At the conclusion of the laser pulse, the front expands freely with a velocity, v_o, defined by a linear trajectory [see Region I of Fig. 11(a)]. The plume begins to slow as the highest velocity components contact the background gas. Under vacuum conditions, the plume intensity is relatively weak, lacks a well-defined contact front, and the front continues to propagate as a free expansion with constant velocity. The mean free path between collisions is 0.2–4 mm for pressures of 50–1000 mTorr, and this contact front between the expanding plume and the background gas quickly becomes apparent. The expanding plume acts as a mechanical piston, compressing the background gas, resulting in the formation of a shock front toward the end of this region. Region II marks the trajectory of a well-developed shock front. The shock dynamics can be described by the Sedov–Taylor theory[52] during this period when the shock is strong. At longer times (Region III), the emissive plume approaches a stopping distance of 3 cm and separates from the weakened shock that approaches M = 1. Three approaches to defining the plume energy dynamics are now pursued using free expansion, blast theory, and a drag model.

A free expansion model is adequate for characterizing the ablation data in vacuum throughout the entire expansion [Fig. 11(b)]. At higher background pressures, a linear trajectory is observed for only the first ~200 ns after which collisions begin to slow the plume. The free expansion velocity for Al in Fig. 11(a) is 1.81 ± .07 cm/μs and for Ti in Fig. 11(b) of 1.57 ± 0.02 cm/μs. These initial free expansion velocities are independent of pressure, varying by ±3% and exhibiting no systematic trends. The free expansion velocities correspond to 61.1 eV per Ti atom and 45.8 eV per Al atom. Considering the mass results from Sec. III A, the plume kinetic energies range from 46 to 78 mJ for Ti ablation and 51–69 mJ for Al ablation for Ar pressures ranging from 1 to 0 Torr. The result that the pressure dependence for total kinetic energy scales directly with the ablated mass leads to a primary conclusion:

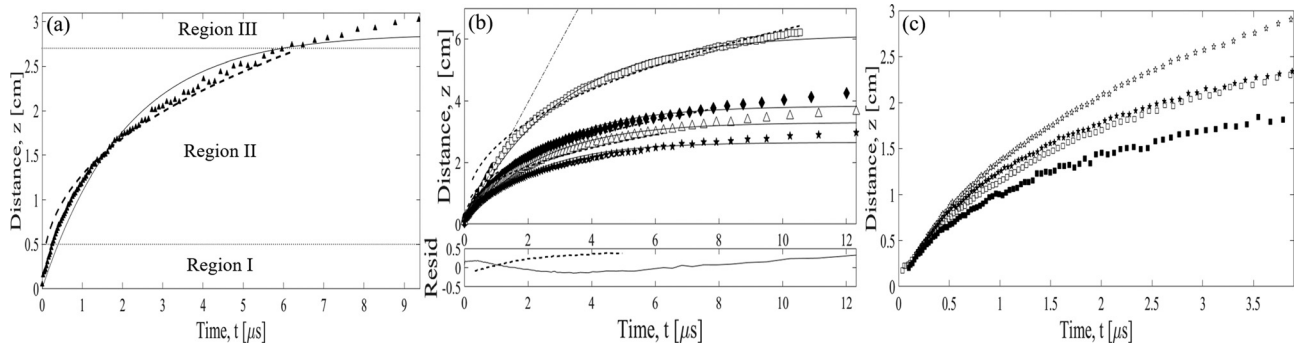

FIG. 11. (a) Trajectory of Al plume from 240 mJ/pulse ablation in 500 mTorr Ar. Region I is the trajectory in which free expansion occurs and the shock wave is forming. Region II is the trajectory in which the shock wave is fully formed and Sedov–Taylor theory is applicable. Region III is the trajectory in which the contact front slows and the shock wave moves ahead of the contact front, (b) Ti blast model (––) and drag model (–) fits to broadband signal as a function of background pressure at (●) vacuum, (□) 50 mTorr, (◆) 250 mTorr, (△) 500 mTorr, and (★) 1000 mTorr and a laser energy of 240 mJ/pulse. A linear, free expansion model (–) fit to the vacuum data is provided for reference and residuals for the 1000 mTorr Sedov–Taylor, and drag model fits are provided in the bottom window, and (c) dependence of plume trajectory on laser pulse energy for (■) Al 174 mJ/pulse, (★) Al 282 mJ/pulse, (□) Ti 174 mJ/pulse, and (☆) Ti 282 mJ/pulse at a background pressure of 500 mTorr.

the fraction of the incident laser energy coupled to both the target and plume decreases at higher background pressures. This result suggests that the extra energy deposited due to greater plume shielding at higher pressure is re-radiated rather than collisionally relaxed. For the ablation conditions in this study, the collision frequency is $\sim 10^7\ s^{-1}$, comparable to the radiative rates. Electron radiative recombination might also increase at higher pressure. Additionally, reflection of the incident laser radiation due to an index of refraction difference at the shock front is possibly enhanced with increasing ambient pressure.

If it is assumed that the available energy above the threshold energy and not observed as kinetic energy is portioned to internal energy, maximum temperatures of ~41 eV/atom for Ti and ~31 eV/atom for Al can be extracted. The internal energy (electronic excitation) is certainly less due to incomplete coupling of the laser energy to both the target and the plume.

Figure 11(c) indicates that the Al and Ti plumes for 500 mTorr argon background travel nearly the same distances for the first 800 ns for 282 mJ/pulse and for the first 400 ns for 174 mJ/pulse. The plume velocity of both species increases with laser energy. The free expansion velocity increases by 14% for both species as the laser energy increases from 174 to 282 mJ/pulse.

A model based on a classical linear drag force is often used to determine the contact front location at which the expanding plume stops, z_f[2]

$$z = z_f\left(1 - e^{-kt}\right), \tag{2}$$

where the deceleration is characterized with a drag decay constant, k. The drag model also provides another estimate of the initial velocity, $v_{0,D} = kz_f$. A fit of Eq. (2) to the data in Fig. 11(a) yields a stopping distance of $z_f = 2.86 \pm 0.04$ cm for Al in 500 mTorr of argon. The dependence of the drag parameters on background pressure and laser energy is further detailed in Fig. 12. The initial velocity of the plume increases with increasing laser energy, reflecting the fact that more energy is available to the expanding plume. The drag model initial velocity at the lowest pressure (50 mTorr) for Ti is $v_{0,D} = 2.12 \pm 0.04$ cm/μs, apparently greater than that of the Ti free expansion value in Fig. 11. We interpret this observation as a difference in weighting and poorer fit residuals for the drag model. Contrary to the initial velocity dependence determined using the free-expansion model, as the pressure is increased, the velocities of Ti and Al decrease from 1.6 cm/μs at 250 mTorr to 1.3 cm/μs at 1000 mTorr. One might not expect the initial drag velocity to depend on the background pressure, but instead to be equivalent to the free-expansion values reported earlier. Drag model fitting to emission images is common[2,26,27] and in the case of $YBa_2Cu_3O_{7-x}$, also show a decrease in drag fitted initial velocity with increasing background pressure.[7] Based on the experimental trajectory evidence, we prefer the early free expansion fits for estimating the plume initial velocity. Constraining the fit of Eq. (2) using

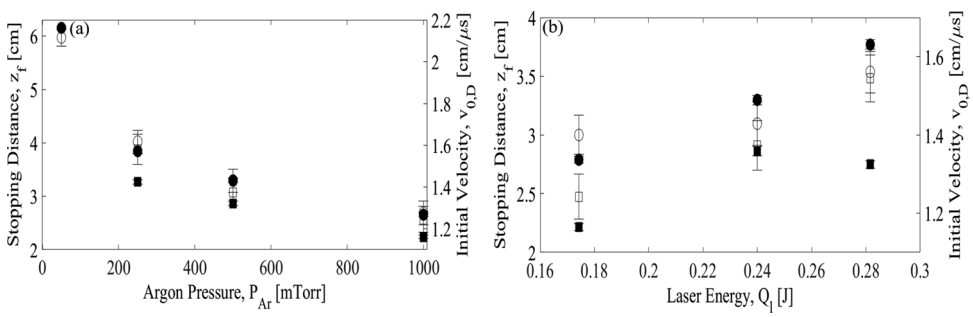

FIG. 12. Dependence of stopping distance, z_f, for (●) Ti and (■) Al and dependence of initial velocity, $v_{o,D}$, for (○) Ti and (□) Al on (a) background pressure, P_b, at 240 mJ/pulse and (b) laser energy, Q_l, at 500 mTorr.

the measured free expansion, velocity produces unacceptably large residuals. The drag model fits are heavily weighted for longer times where significant collisions occur and is best suited for estimating stopping distances. The stopping distances, z_f, are larger for Ti on average by 0.5 cm, consistent with the greater Ti momentum. Stopping distance is shorter at higher pressure due to the increase in collision frequency. The stopping distances also generally increase with higher laser energy due to the higher initial velocity. An evaluation of the shock energy in Region II of Fig. 11(a) using the blast model is now accomplished.

The emissive plume front trajectories may be further interpreted through the use of a Sedov–Taylor point blast model. The Sedov–Taylor model [Eq. (3)] describes a shock wave produced after an instantaneous point detonation, relating the shock energy, E_{ST}, the background gas density, ρ, the plume dimensionality, n ($n=1$ for planar expansion, $n=2$ for cylindrical, and $n=3$ for spherical), a constant factor dependent on the ratio of specific heats [$\xi = 1.49\,(n=1)$, $\xi = 1.77\,(n=2)$, and $\xi = 1.15\,(n=3)$], and time, t, to the shock front location at a distance from the target z[52,55]

$$z = \xi\left(\frac{E_{ST}}{\rho}\right)^{\frac{1}{n+2}} t^{\frac{2}{n+2}}. \tag{3}$$

This model is relevant when the amount of mass displaced by the expanding shock front is larger than the amount of mass in the expanding shockwave and when the pressure behind the shock front is larger than the pressure of the background gas[52,56]

$$z_L = \left(\frac{3m_a}{2\pi\rho}\right)^{\frac{1}{3}} \ll z \ll \left(\frac{2E_a}{P_b}\right)^{\frac{1}{3}} = z_H, \tag{4}$$

where m_a is the amount of mass ablated from the surface, ρ is the background gas density, E_a is the initial ablation energy (laser energy), and P_b is the background gas pressure. The lower bound limit is estimated from the ablated mass reported in Sec. III A and is typically 0.3–1.4 cm. For the Al 500 mTorr example in Fig. 11(a), this limit is achieved for $t > 0.255\ \mu$s. During the earlier times, the blast theory unrealistically predicts velocities that exceed the free expansion and become very large at $t=0$. Fits of the blast model is illustrated in Fig. 11(b) and does not include data below the lower bounds of 1.4 cm for 50 mTorr, 0.76 cm for 250 mTorr, and 0.5 cm for 500 and 1000 mTorr.

The high limit of Eq. (4) ranges from 14 to 44 cm, well beyond the observed stopping distances. Apparently, the emissive plume detaches from the shock front propagating in the background gas well before the upper bound. The ICCD images observe the visible emissions only from excited constituents and any non-excited constituents cannot be observed. At atmospheric pressures, the emissive plume exhibits a stopping distance, where shadowgraphy indicates that the non-emissive shock front separates from the emissive plume and continues to propagate in accordance with the blast model.[17,18] Because the location of the shock front as it breaks away from the emissive plume is not observed in this study, the upper bound described in Eq. (4) must be further limited. Harilal *et al.* determined a breakaway time of ~400 ns from ablation of Al in argon at atmospheric pressure.[18] This breakaway time is converted to a non-dimensional time according to $\tau = v_{Ar}\left(\frac{2E_a}{P_b}\right)^{\frac{1}{3}} t$, and used to determine the corresponding limiting times and locations for the studied laser energy and background pressure conditions. Breakaway locations, z_B, of 6.20, 3.76, 2.99, and 2.30 cm for Ti ablation in 50, 250, 500, and 1000 mTorr argon, respectively, and of 3.03, 2.40, and 1.80 cm for Al ablation in 250, 500, and 1000 mTorr argon, respectively, were determined using this scaling. These calculated values for z_B served as the upper bound for fitting Eq. (3) to the emissive plume trajectories.

Typical fits to the blast and drag models are compared in Fig. 11(b). In general, the drag model fits are marginally superior to the blast model for Ti, while the blast model fits are superior for Al trajectories. The largest residual root mean square error (RMSE) of 0.185 cm was calculated for 50 mTorr Ti ablation fit with the blast model, while the largest RMSE for Al was 0.152 cm for 250 mTorr fit to the drag model. As others have observed, the drag model fit residuals show smaller residuals for lower background pressure.[2] Structure above the noise in the data is present for both the blast and drag fits, indicating systematic problems with both the models.

A comparison of the blast fit parameters as functions of laser energy and pressure are observed in Fig. 13. Analysis of the optimal plume dimensionality reveals that the Ti and Al plume dimensionalities are less than spherical for all pressures, ranging from 1.7 ± 0.1 to 2.9 ± 0.1. Furthermore, plume dimensionality changes very little with changing fluence, with the Al plume dimensionality higher on average ($n = 2.3 \pm 0.1$) than the Ti average plume dimensionality

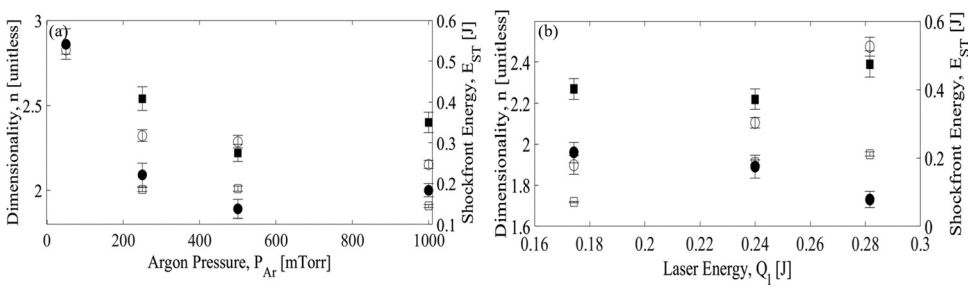

FIG. 13. Dependence of plume dimensionality, n, for (●) Ti and (■) Al and dependence of plume front energy, E_{ST}, for (○) Ti and (□) Al on (a) background pressure, P_b, at 218 mJ/pulse and (b) laser energy, Q_l, at 500 mTorr. E_{ST} was determined using $n=3$.

($n = 1.9 \pm 0.1$). Deviations from spherical expansion are likely due in part to the absence of a point source.

The fits for the shock front energy, E_{ST}, using $n = 3$, for Ti at 240 mJ/pulse decrease from 528 ± 10 mJ at 50 mTorr to 247 ± 10 mJ at 1 Torr. Due to the target plane, the laser plume is only a hemispherical expansion, whereas the blast theory assumes expansion in both $\pm z$ directions. Therefore, the blast theory fit parameter for energy is reduced by a factor of two to characterize the shock energy.[57] The resulting Ti energies from the blast model, $E_{ST}/2$, are 51%–100% of the incident laser energy. For aluminum the shock front coupling is somewhat less, 27%–38%. If the threshold energies listed in Table II are considered, the Sedov-Taylor model overestimates the Ti energy in the plume, predicting 120% of the available energy in the shock front for 500 mTorr Ar ablation while Sedov-Taylor estimates ~90% of the available energy in the Al shock front for 1000 mTorr Ar ablation. Conservation of energy does not allow the Sedov-Taylor energy to be above 100% of the available energy.

A powerful concept of self-similarity that comprises the Sedov-Taylor model enables the trajectories to be scaled for comparison between various energies and background pressures using the Sedov-Taylor limits from Eq. (4). Figure 14 shows the trajectory data from Fig. 11(b) scaled using these limits. The similarity between various background pressures is only modest and a single trajectory for all conditions is not achieved. This scaling assumes a constant $n = 3$ spherical expansion, but the fits of Fig. 13 yield $n < 3$ with a significant dependence on pressure. The different degree of curvature in the trajectories at various pressures reflects this change in expansion dimensionality. Furthermore, the variation in E_{ST} with pressure conflicts with the pressure similarity. The decrease in initial ablation energy released at higher pressure is consistent with the decrease in plume kinetic energy derived from the free expansion velocity and mass measurements and supports the conclusion that laser coupling to both the target and plume decreases at higher pressure. While the shielding mechanism is not fully evident, it appears that plume radiation might increase at higher pressure.

The plume dynamics energy distribution may be best summarized by a discussion of the regions labeled in Fig. 11(a). Threshold energies determined in Sec. III A reveal that ≤48% and ≤63% of the original 240 mJ are available to produce and drive the observed Al and Ti ablated plumes, respectively. In Region I after termination of the laser pulse, free expansion velocities yield vacuum kinetic energies of $61 \pm 11\%$ and $52 \pm 12\%$ of the available Al and Ti energy (for the remainder of this discussion, "available energy" will refer to energy above the threshold values given in Sec. III A), respectively, with the remaining energy going into the internal energy of the plume. With increasing background pressure, the laser is partially shielded from the target and the plume interacts with the ambient gas through collisions slowing the expansion of the plume and transferring kinetic energy into internal energy, with only $61 \pm 3\%$ and $58 \pm 17\%$ of the available energy going into kinetic energy in 1 Torr of argon for Ti and Al, respectively. As the plume continues to expand, it piles up at the contact front and compresses the background gas further, forming a strong shock wave as Region I transitions to Region II. Application of the Sedov–Taylor blast model to the trajectory in Region II reveals that up to 90% of the available energy goes into the Al shock front. With more accurate locations of the contact front-shock front breakaway, it is likely that nearly all of the available energy is located in the Ti shock front as well. Transition from Region II to Region III is described by a decrease in velocity of the emissive plume due to further collisions with the background gas while the shockwave breaks away and propagates at a higher velocity. We can only observe the emissive plume in this region and so no quantitative measure of the available energy can be made.

IV. CONCLUSION

The plume dynamics of Al and Ti under UV, 25 ns ablation at up to 3.5 J/cm^2 have been compared by measuring the mass ablated and imaging the plume dynamics. Mass loss results are consistent with modest ablation thresholds of 90 and 126 mJ/pulse for Ti and Al, respectively. The ionized plume partially shields the surface, allowing additional atoms to be ablated at higher laser fluence but shielding the surface more at higher background pressure. The plume kinetic energy is very high, 45–61 eV/atom, corresponding to 10–13 laser photons per ablated atom. The Sedov–Taylor point blast model shows laser-shock wave coupling of up to 40% of the incoming energy for Al ablation. Aluminum exhibits a slightly higher expansion velocity than Ti due to lower mass but approximately the same initial kinetic energy. The Al plumes also

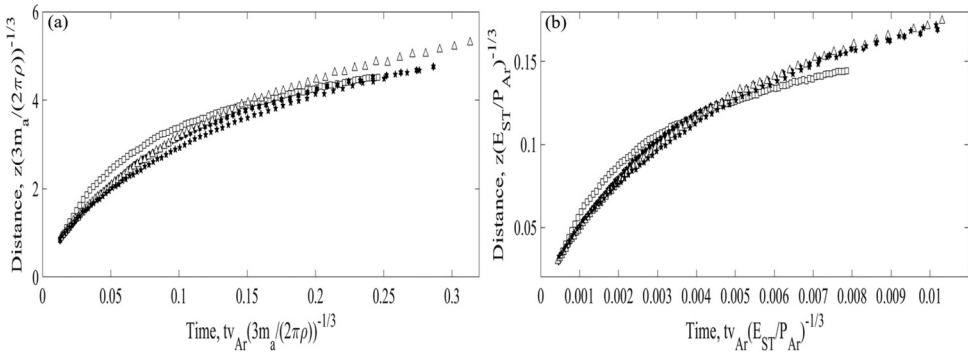

FIG. 14. Ti trajectory data for (□) 50 mTorr, (★) 250 mTorr, (△) 500 mTorr, and (★) 1000 mTorr and a laser energy of 240 mJ/pulse scaled using (a) the lower limit of Eq. (4), and (b) using the upper limit of Eq. (4).

decelerate relatively more quickly due to the lower momentum. Further experimental studies need to be performed to better determine the location of contact front-shock front breakaway and to better determine the actual amount of redeposited material back onto the surface for the conditions present in this paper. The present survey of plume dynamics is necessary for a detailed study of shock strength and shock front instabilities and for characterizing the evolution of forward directed speed distributions.

ACKNOWLEDGMENTS

This work was partially supported by the Air Force Office of Scientific Research under task LRIR #14RQ08COR.

[1]D. Bauerle, *Laser Processing and Chemistry*, 3rd ed. (Springer, Berlin, 2000).
[2]D. B. Chrisey and G. K. Hubler, *Pulsed Laser Deposition of Thin Films* (John Wiley & Sons, Inc., New York, 1994).
[3]A. De Giacomo, M. Dell'Aglio, O. De Pascale, R. Gaudiuso, V. Palleschi, C. Parigger, and A. Woods, Spectrochim. Acta, Part B: At. Spectrosc. **100**, 180 (2014).
[4]D. B. Geohegan and A. A. Puretzky, Appl. Phys. Lett. **67**, 197 (1995).
[5]S. S. Chu and C. P. Grigoropoulos, J. Heat Transfer **122**, 771 (2000).
[6]E. Millon, O. Albert, J. C. Loulergue, J. Etchepare, D. Hulin, W. Seiler, and J. Perrière, J. Appl. Phys. **88**, 6937 (2000).
[7]C. Phelps, C. J. Druffner, G. P. Perram, and R. R. Biggers, J. Phys. D: Appl. Phys. **40**, 4447 (2007).
[8]V. C. Dinca, S. Soare, A. Barbalat, C. Z. Dinu, A. Moldovan, I. Stoica, T. Vassu, A. Purice, N. Scarisoareanu, R. Birjega, V. Craciun, V. F. DeStefano, and M. Dinescu, Appl. Surf. Sci. **252**, 4619 (2006).
[9]Y. Suda, H. Kawasaki, T. Ueda, and T. Ohshima, Thin Solid Films **453–454**, 162 (2004).
[10]M. Ye and C. P. Grigoropoulos, J. Appl. Phys. **89**, 5183 (2001).
[11]S. Eliezer, N. Eliaz, E. Grossman, D. Fisher, I. Gouzman, Z. Henis, S. Pecker, Y. Horovitz, M. Fraenkel, S. Maman, and Y. Lereah, Phys. Rev. B: Condens. Matter Mater. Phys. **69**, 144119 (2004).
[12]S. Amoruso, R. Bruzzese, N. Spinelli, R. Velotta, M. Vitiello, X. W. Ausanio, V. Iannotti, and L. Lanotte, Appl. Phys. Lett. **84**, 4502 (2004).
[13]S. Amoruso, M. Armenante, V. Berardi, R. Bruzzese, and N. Spinelli, Appl. Phys. A: Mater. Sci. Process. **65**, 265 (1997).
[14]P. R. Willmott and J. R. Huber, Rev. Mod. Phys. **72**, 315 (2000).
[15]G. P. Perram, S. Cusumano, R. L. Hengehold, and S. T. Fiorino, *Introduction to Laser Weapon Systems* (Directed Energy Professional Society, Albuquerque, 2010).
[16]W. M. Steen and J. Mazumder, *Laser Material Processing*, 4th ed. (Springer, New York, 2010).
[17]G. Callies, P. Berger, and H. Hugel, J. Phys. D: Appl. Phys. **28**, 794 (1995).
[18]S. S. Harilal, G. V. Miloshevsky, P. K. Diwakar, N. L. Lahaye, and A. Hassanein, Phys. Plasmas **19**, 083504 (2012).
[19]A. De Giacomo, Spectrochim. Acta, Part B: At. Spectrosc. **58**, 71 (2003).
[20]N. M. Shaikh, S. Hafeez, B. Rashid, and M. A. Baig, Eur. Phys. J. D **44**, 371 (2007).
[21]G. Abdellatif and H. Imam, Spectrochim. Acta, Part B **57**, 1155 (2002).
[22]S. S. Harilal, B. O'Shay, Y. Tao, and M. S. Tillack, J. Appl. Phys. **99**, 083303 (2006).
[23]N. Farid, S. S. Harilal, H. Ding, and A. Hassanein, J. Appl. Phys. **115**, 033107 (2014).
[24]L. Torrisi, D. Margarone, A. Borrielli, and F. Caridi, Appl. Surf. Sci. **254**, 4007 (2008).
[25]K. Sasaki, S. Matsui, H. Ito, and K. Kadota, J. Appl. Phys. **92**, 6471 (2002).
[26]D. B. Geohegan, Appl. Phys. Lett. **60**, 2732 (1992).
[27]S. S. Harilal, C. V. Bindhu, M. S. Tillack, F. Najmabadi, and A. C. Gaeris, J. Appl. Phys. **93**, 2380 (2003).
[28]A. E. Hussein, P. K. Diwakar, S. S. Harilal, and A. Hassanein, J. Appl. Phys. **113**, 143305 (2013).
[29]A. K. Sharma and R. K. Thareja, Appl. Surf. Sci. **243**, 68 (2005).
[30]W. F. Luo, X. X. Zhao, Q. B. Sun, C. X. Gao, J. Tang, H. J. Wang, and W. Zhao, Pramana-J. Phys. **74**, 945 (2010).
[31]P. Écija, M. N. S. Rayo, R. Martínez, B. Sierra, C. Redondo, F. J. Basterretxea, and F. Castaño, Phys. Rev. A **77**, 032904 (2008).
[32]G. Baraldi, A. Perea, and C. N. Afonso, Appl. Phys. A: Mater. Sci. Process. **105**, 75 (2011).
[33]V. Y. Baranov, O. N. Derkach, V. G. Grishina, M. F. Kanevskii, and A. Y. Sebrant, Phys. Rev. E **48**, 1324 (1993).
[34]S. Amoruso, V. Berardi, R. Bruzzese, R. Capobianco, R. Velotta, and M. Armenante, Appl. Phys. A: Mater. Sci. Process. **62**, 533 (1996).
[35]O. Albert, S. Roger, Y. Glinec, J. C. Loulergue, J. Etchepare, C. Boulmer-Leborgne, J. Perriere, and E. Millon, Appl. Phys. A: Mater. Sci. Process. **76**, 319 (2003).
[36]S. S. Harilal, C. V. Bindhu, M. S. Tillack, F. Najmabadi, and A. C. Gaeris, J. Phys. D: Appl. Phys. **35**, 2935 (2002).
[37]A. A. I. Khalil, M. Richardson, L. Johnson, and M. A. Gondal, Laser Phys. **19**, 1981 (2009).
[38]W. Bauer, G. Perram, and T. Haugan, SPIE Conf. Proc. **2016**, 100140S.
[39]W. M. Haynes, *CRC Handbook of Chemistry and Physics*, 93rd ed. (CRC Press, Taylor and Frances Group, Boca Raton, FL, 2012).
[40]A. Kramida, Y. Ralchenko, J. Reader, and NIST Atomic Spectra Database Team, see http://physics.nist.gov/asd for National Institute of Standards and Technology, Gaithersburg, MD (2015).
[41]W. Sdorra, J. Brust, and K. Niemax, Mikrochim. Acta **108**, 1 (1992).
[42]Y. Iida, Spectrochim. Acta, Part B: At. Spectrosc. **45**, 1353 (1990).
[43]L. Torrisi, G. Ciavola, S. Gammino, L. Ando, A. Barna, L. Laska, and J. Krasa, Rev. Sci. Instrum. **71**, 4330 (2000).
[44]R. Timm, P. R. Willmott, and J. R. Huber, J. Appl. Phys. **80**, 1794 (1996).
[45]N. Arnold, B. Luk'yanchuk, and N. Bityurin, Appl. Surf. Sci. **127–129**, 184 (1998).
[46]L. Torrisi, F. Caridi, A. Picciotto, and A. Borrielli, Nucl. Instrum. Methods Phys. Res. B **252**, 183 (2006).
[47]L. M. Cabalin and J. J. Laserna, Spectrochim. Acta, Part B **53**, 723 (1998).
[48]W. Sdorra and K. Niemax, Mikrochim. Acta **107**, 319 (1992).
[49]S. Preuss, A. Demchuk, and M. Stuke, Appl. Phys. A: Mater. Sci. Process. **61**, 33 (1995).
[50]C. J. Druffner, G. P. Perram, and R. R. Biggers, Rev. Sci. Instrum. **76**, 93101 (2005).
[51]F. Claeyssens, S. J. Henley, and M. N. R. Ashfold, J. Appl. Phys. **94**, 2203 (2003).
[52]Y. B. Zel'dovich and Y. P. Raizer, *Physics of Shock Waves and High-Temperature Hydrodynamic Phenomena* (Dover Books, New York, 2002).
[53]A. De Giacomo, M. Dell'Aglio, D. Bruno, R. Gaudiuso, and O. De Pascale, Spectrochim. Acta, Part B: At. Spectrosc. **63**, 805 (2008).
[54]A. Vertes, R. Gijbels, and F. Adams, "Laser ionization mass analysis," in *Chemical Analysis* (John Wiley & Sons, Inc., New York, 1993), Vol. 124.
[55]D. L. Jones, National Bureau of Standards Technical Note 155 the Energy Parameter B for Strong Blast Waves, Boulder, CO, 1962.
[56]A. Misra, A. Mitra, and R. K. Thareja, Appl. Phys. Lett. **74**, 929 (1999).
[57]R. B. Hall, J. Appl. Phys. **40**, 1941 (1969).